









Thermodynamic Structure of the Solar Corona: Tomographic Reconstructions and MHD Modeling

Diego G. Lloveras¹  · Alberto
M. Vásquez^{1,2}  · Federico A. Nuevo^{1,3}  ·
Cecilia Mac Cormack^{1,2}  ·
Nishtha Sachdeva⁴  · Ward Manchester
IV⁴  · Bartholomeus Van der Holst⁴  ·
Richard A. Frazin⁴ 

© Springer

Abstract Observational techniques play an essential role in advancing our understanding of the physics of the solar corona. They provide validation data

-
- ✉ D.G. Lloveras
dlloveras@iafe.uba.ar
 - ✉ A.M. Vásquez
albert@iafe.uba.ar
 - ✉ F.A. Nuevo
federico@iafe.uba.ar
 - ✉ C. Mac Cormack
cmaccormack@iafe.uba.ar
 - ✉ N. Sachdeva
nishthas@umich.edu
 - ✉ W. Manchester IV
chipm@umich.edu
 - ✉ B. Van der Holst
bartvand@umich.edu
 - ✉ R.A. Frazin
rfrazin@umich.edu

- ¹ Instituto de Astronomía y Física del Espacio (IAFE), CONICET-UBA, CC 67 - Suc 28, (C1428ZAA) Ciudad Autónoma de Buenos Aires, Argentina
- ² Universidad Nacional de Tres de Febrero (UNTREF). Departamento de Ciencia y Tecnología, Sáenz Peña, Argentina.
- ³ Ciclo Básico Común (CBC), Universidad de Buenos Aires (UBA), Buenos Aires, Argentina
- ⁴ Department of Climate and Space Sciences and Engineering (CLaSP), University of Michigan, 2455 Hayward Street, Ann Arbor, MI 48109-2143, USA

for three-dimensional (3D) magnetohydrodynamic (MHD) models of the solar atmosphere, key to improve their space weather forecasting capabilities. Solar rotational tomography (SRT) is currently the sole observational technique that provides an empirical 3D description of some of the fundamental plasma parameters of the solar corona at a global scale. Based on EUV data of space borne instruments, differential emission measure tomography (DEMT) allows constructing 3D maps of the coronal electron density and temperature at heliocentric heights below 1.25 R_{sun}. We carry out a study of the corona combining DEMT reconstructions with MHD simulations using the latest version of the Alfvén Wave Solar Model (AWSoM) of the Space Weather Modeling Framework (SWMF). Target rotations were selected from the solar minimum between solar cycles (SC) 23 and 24 and the declining phase of SC 24. The 3D tomographic and MHD models are analysed and compared in distinct coronal magnetic structures. We report in quantitative detail on the 3D thermodynamic structure of the inner corona as revealed by the DEMT analysis. We show in particular the existence of diverse types of temperature structures in the low and mid latitudes of the streamer belt, and that the heating energy required to keep them stable may be accounted for by Alfvén waves. We show that the latest version of the AWSoM model results agree with DEMT reconstructions to within a $\approx 20\%$ accuracy or better. We report on aspects of the AWSoM model that could be improved to better reproduce the DEMT results, in particular concerning the source region of the fast/slow solar winds.

Keywords: Solar Cycle, Observations; Corona,E; Corona, Structures

1. Introduction

Being the place where the solar atmosphere is heated and the solar wind accelerated, and where impulsive events such as solar flares and coronal mass ejections are energized, observation and modeling of the solar corona are tasks of great relevance to improve our understanding of the Sun-Earth environment. To advance our knowledge of the physics of the solar corona, as well as to improve its three-dimensional (3D) models, information derived from observational data plays a key role. Solar rotational tomography is currently the sole observational technique able to provide a quantitative empirical description of the 3D distribution of some fundamental plasma parameters of the solar corona at a global scale.

NOTE: Here we will put in a couple of paragraphs summarizing what SRT and DEMT are, including references and defining the accronyms in the process. We should refer to minima in particular. We should mention the instruments and missions we use as data for DEMT, and define their accronyms too. Also one paragraph on the SWMF/AWSoM model, including references and defining the accronyms on the way.

Based on time-series of EUV images, differential emission measure tomography (DEMT) allows reconstruction of the 3D distribution of the differential emission measure (DEM) of the solar corona. The technique was first developed

by Frazin, Vásquez, and Kamalabadi (2009), and first applied to the observational study of coronal structures by Vásquez, Frazin, and Kamalabadi (2009). In DENT, the low corona in the height range $1.0 - 1.25 R_{\odot}$ is discretized in a spherical computational grid. The size of the tomographic grid cell (or voxel) is typically set to $0.01 R_{\odot}$ in the radial direction and 2° in both the latitudinal and longitudinal directions. The cadence of the data time-series is set to 6 hr. The main product of the technique is the local DEM (LDEM) at each voxel, a measure of the temperature distribution of the plasma contained in it. A recent review by Vásquez (2016) summarizes the DENT works up until then. More recently Lloveras *et al.* (2017) applied DENT to study the last two solar minima, and Mac Cormack *et al.* (2017) developed a new DENT product concerning the energetics of the inner solar corona.

2. Methodology

2.1. DENT Reconstructions

We carried out the 3D DENT reconstruction and MHD modeling of two target Carrington rotations (CR). We selected CR-2082 (2009, 05 April through 03 May), a deep minimum rotation between solar cycles (SC) 23 and 24, and CR-2208 (2018, 02 September through 29 September), a rotation during the early declining phase of SC 24. To study CR-2082 and CR-2208 data taken by the STEREO/EUVI-B and SDO/AIA instruments was used, respectively. The EUVI and AIA data were prepared using the latest processing tools and calibration corrections provided by their teams through the SolarSoft package. For this work, we introduced two improvements in the implementation of the DENT technique, as described next.

While in all previous DENT studies full-disk data was used to perform tomography, in this work we opted to only use off-limb data. In this way, the smallest scale and brighter coronal features seen on disk (most typically in the 171\AA band) are not included. This has two implications. Firstly, the fast dynamics that typically characterizes those structures is absent from the data. Secondly, only half synodic rotation worth of data is needed to constrain the inversion problem for the whole coronal volume. As a result, coronal dynamics induced artifacts are reduced compared to previous DENT reconstructions. . The solution of the tomographic problem involves a very large sparse matrix. Such type of inversion problems are characterized by spurious high-frequency artifacts in the solution, which can be mitigated through *regularization* techniques (Frazin, 2000). In the case of DENT, all previous efforts used the 2D scheme implemented by Frazin, Vásquez, and Kamalabadi (2009), using a finite difference matrix operator to approximate angular derivatives in both latitude and longitude. Also new to the present work, is the implementation of an expanded 3D regularization scheme, which adds to the previous scheme a finite difference matrix operator to approximate radial derivatives. In this way, the tomographic inversion problem is performed penalizing nonphysical high-frequency artifacts in all three spatial directions. As a result, tomographic reconstructions behave more smoothly close

to the radial boundaries of the computational grid when compared to previous reconstructions.

We summarize next the main aspects of DENT required for the analysis of this work. We refer the reader to Frazin, Vásquez, and Kamalabadi (2009) for a full description of the technique.

In a first step, the time series of EUV images is used to solve a solar rotational tomography (SRT) problem, for each EUV band independently. As a result, the 3D distribution of the so called *filter band emissivity* (FBE) is determined for each band separately. The FBE, an emissivity-type quantity, is defined as the wavelength integral of the coronal EUV spectral emissivity and the telescope's passband function of each EUV channel. Line-of-sight (LOS) integration of the FBE provides synthetic images that can be quantitatively compared to the real data in the time series. To find the FBE, the tomographic problem is posed as a global optimization problem in which the quadratic norm of the difference between all pairs of synthetic and real images is minimized.

In a second step, the FBE values obtained for all bands in each voxel of the tomographic grid are used to constrain the determination of the LDEM which, as described in Section 1, describes the temperature distribution of the plasma within the individual voxel. Specifically, at each tomographic voxel i , the FBE of the band k is related to the LDEM of the voxel according to

$$\text{FBE}_i^{(k)} = \int dT \text{LDEM}_i(T) \text{TRF}^{(k)}(T), \quad k = 1, \dots, K \quad (1)$$

where K is the number EUV bands, and $\text{TRF}^{(k)}$ is the *temperature response function* of the j -th detector. The TRFs are here computed based on the (known) channel's passband times the coronal emissivity at that temperature (normalized by the squared electron density). The emissivity model used here is provided by the latest version of the CHIANTI atomic database and plasma emission model (Del Zanna *et al.*, 2015; Landi *et al.*, 2013).

Due to unresolved coronal dynamics, tomographic reconstructions exhibit negative values of the reconstructed FBE, or zero when the solution is constrained to positive values (Frazin, 2000; Frazin, Vásquez, and Kamalabadi, 2009). These non-reconstructed voxels are indicated in black color in the latitude-longitude (Carrington) maps of DENT results in Section 3.

In the present work, data from 3 EUV bands was used. 171, 193 and 211 Å in case of AIA, and 171, 195 and 284 Å bands in case of EUVI. When using data from 3 EUV bands, a Gaussian model for the LDEM is able to accurately predict the tomographic emissivities (Frazin, Vásquez, and Kamalabadi, 2009; Nuevo *et al.*, 2015). In each tomographic voxel the problem is then reduced to finding the values of the three free parameters of the Gaussian (centroid, standard deviation, and area) that allow to best reproduce the three tomographically reconstructed values of FBE in that voxel.

Once the LDEM is determined at each voxel, the LDEM-averaged squared electron density N_m^2 and electron temperature T_m in the voxel can be computed by taking its zeroth and first moments over temperature. More specifically, at

the i -th voxel,

$$N_{\text{m},i}^2 = \langle N_{\text{e}}^2 \rangle_i = \int dT \text{LDEM}_i(T), \quad (2)$$

$$T_{\text{m},i} = \langle T_{\text{e}} \rangle_i = \frac{1}{\langle N_{\text{e}}^2 \rangle_i} \int dT T \text{LDEM}_i(T), \quad (3)$$

We define next a measure of the accuracy of the LDEM model to predict the tomographic FBEs in each voxel, as

$$R_i \equiv (1/K) \sum_{k=1}^K \left| 1 - \text{FBE}_{i,\text{syn}}^{(k)} / \text{FBE}_{i,\text{tom}}^{(k)} \right|, \quad (4)$$

being the average relative difference between the tomographic and the synthetic FBEs. The final product of DMT is in the form of 3D maps of the LDEM-averaged quantities $\sqrt{N_{\text{m}}^2}$ and T_{m} , as well as of the measure R .

2.2. AWSoM Simulations

NOTE: This section will summarize the AWSoM model. Chip, Nishtha, do you think you could provide 2 or 3 paragraphs? We believe the points to cover are:

- Data input. Link with the data input for DMT in terms of dates, etc. One paragraph.
- Main physical and technical aspects (grid in particular) of the model. One paragraph.
- Explain the artificially extended TR. One paragraph.
- What are the products of the model we care about in this paper (N_{e} , T_{e} , B , V , as of now). One paragraph.

In the transition region (TR), the plasma heats up and becomes less dense by several orders of magnitude over a short distance. Modeling this region realistically has a very high computational cost. For this reason, the model uses an artificially extended TR about $\approx 0.05 R_{\odot}$ thick, as well as artificially large values for the electronic density and temperature as boundary conditions in $r = 1 R_{\odot}$. Consequently, model results below $\approx 1.05 R_{\odot}$ were not taken into account in this article.

2.3. Tracing Results Along Magnetic Fieldlines

To determine the electron density and temperature along individual magnetic field lines, first both the thermodynamic results and the magnetic field obtained with the AWSoM model were interpolated into the DMT grid. Then, the geometry of the field lines is determined by numerical integration of the first order differential equations $dr/B_r = r d\theta/B_{\theta} = r \sin(\theta) d\phi/B_{\phi}$, both inwards and outwards, from the specified 3D coordinates of a starting point. In order

to evenly sample the whole volume spanned by the DENT reconstructions, one starting point is selected at the center of each tomographic cell at 6 uniformly spaced heights, ranging from 1.025 to $1.225 R_{\odot}$, and every 2° in both latitude and longitude, for a total of 96,000 starting points.

For analysis purposes, the traced magnetic field lines are classified as open or closed according to their full geometry. Each closed field line is further classified as “small” or “large”, according to its coronal length L being respectively smaller or larger than the median value of the whole population, which is $\text{Md}(L) \approx 0.5 R_{\odot}$ for both rotations. Finally, each closed magnetic field line is separated in its two “legs”, defined as the two segments that go from each of its two footpoints (i.e. their location at $r = 1 R_{\odot}$) to its apex (i.e., the location of maximum height).

At this stage, DENT and AWSOM products can be traced along open and closed magnetic field lines. Once the field line geometry is computed in high spatial resolution, only one sample point per tomographic cell is kept (the median one). To each sample point, the results corresponding to the tomographic voxel where it is located are assigned to it. As a result, for each field line one data point per tomographic cell is obtained. This approach was firstly used by Huang *et al.* (2012) to study temperature structures in the solar minimum corona and by Nuevo *et al.* (2013) to expand that analysis to rotations with different level of activity.

For each open field line and for each closed field leg, an exponential fit was applied to the electron density data points and a linear fit applied to the electron temperature data points. For the DENT model the data points used were $\sqrt{N_m^2(r)}$ and $T_m(r)$, and in case of the AWSOM models the data points used were $N_e(r)$ and $T_e(r)$. The exponential and linear fit equations are described by

$$\sqrt{N_m^2} = N_0 \exp[-(h/\lambda_N) / (r/R_{\odot})] \quad (5)$$

$$T_m = T_0 + m h \quad (6)$$

where $h \equiv r - 1 R_{\odot}$ is the coronal height measured from the photosphere. In the electron density fit, $\lambda_N [R_{\odot}]$ is the density scale height and $N_0 [\text{cm}^{-3}]$ is the electron density at the footpoint ($h = 0$) of the loop. In the electron temperature fit, $m [\text{MK}/R_{\odot}]$ is the slope and $T_0 [\text{MK}]$ is the electron temperature at the footpoint of the loop. The slope m is the radial gradient of the electron temperature along the loop, which we denote as $m = \nabla_r T_m$ hereafter, being $\nabla_r \equiv \mathbf{e}_r \cdot \nabla$ the radial derivative operator, where \mathbf{e}_r is the heliocentric radial unit vector.

In the case of the electron density, the fitted function corresponds to the isothermal hydrostatic equilibrium solution, allowing for variation of the solar gravitational acceleration with height. This choice of function provides a straightforward means to directly evaluate how compatible is the observed coronal thermodynamical state with the hydrostatic solution.

Coronal magnetic structures for which temperature increases/decreases with height (in the inner corona) were dubbed as “up”/“down” loops by Huang *et al.* (2012) and Nuevo *et al.* (2013), who first reported their presence by means of DENT studies. As speculated by the authors of those works, loops of type down can be expected if the heating deposition is strongly confined near the coronal

base of a magnetic loop. Down loops were first predicted by Serio *et al.* (1981), and later on by Aschwanden and Schrijver (2002). In a recent study, Schiff and Cranmer (2016) reproduced both down and up loops by means of numerical simulations, using a 1D steady-state model and considering time-averaged heating rates. **NOTE: Modifiqué la descripción del test estadístico en el próximo párrafo . Estuve leyendo un poco y hay que asegurarse que esto quede escrito bien. Yo busqué la frase más vaga que me parece tiene un sentido científico claro. Aquí hay una versión de divulgación:**

www.statisticshowto.datasciencecentral.com/confidence-level/ pero tener cuidado con esto: busquen “Statistical Significance” en la Wikipedia, y lea la breve sección “Redefining significance” al final del artículo.

To determine if the leg of a traced field line is of type up or down, we first determine the Pearson correlation coefficient $\rho(T, r)$ between the DENT temperature T_m and the heliocentric height r data points. We then select field lines for which the temperature is significantly correlated with height by requiring $|\rho(T, r)| > 0.5$. To test the goodness of the fit to the temperature-height data we perform a chi-squared test (Press *et al.*, 2002) considering the uncertainty of the DENT data points, selecting legs for which the fit matches the data with a 90% confidence level. In this way, legs for which the DENT temperature does not show a significant correlation with height, or the linear fit to temperature is not good enough, are excluded from the analysis. The test is also applied to the density-height data points, to ensure the trend is reasonably represented by the exponential fit. Finally, selected legs are then classified as up or down according to if $\nabla_r T_m > 0$ or $\nabla_r T_m < 0$, respectively. The linear fit allows characterization of the variation of T_m with height by means of a characteristic temperature gradient $\nabla_r T_m$ [MK/R_⊙] along each leg. The chi-squared test to evaluate the quality of the fits considers the uncertainty level in the DENT products due to systematic sources (radiometric calibration and tomographic regularization), that Lloveras *et al.* (2017) estimated to be $\Delta T_m \approx 10\%$ and $\Delta \sqrt{N_m^2} \approx 5\%$. In summary, to be selected a leg must meet all three following conditions:

- i) The leg must go through at least five tomographic grid cells with reconstructed data, and there must be at least one data point in each third of the range of heights spanned by the leg. This requirement is set to ensure a reasonably spread sample of heights along the leg.
- ii) The DENT temperature and height data points must meet $|\rho(T, r)| > 0.5$.
- iii) The confidence level of both the exponential and linear fits must be larger than 90%.

To characterize the global thermodynamic state of the inner solar corona in distinct magnetic structures, the DENT and AWSOM results were traced along the magnetic field lines of the latter model. Based on the geometry and size of the loops, as well as on their thermodynamical properties, their legs were classified in four different types in this work:

- Type 0: closed-small-down with footpoints in the range $|\text{latitude}| < 50^\circ$.
- Type I: closed-small-up with footpoints in the range $|\text{latitude}| < 50^\circ$.
- Type II: closed-large-up with footpoints in the range $|\text{latitude}| > 40^\circ$.

- Type III: open with footpoint in the range $|\text{latitude}| > 60^\circ$.

Legs of type down turn out to have a significant population only for closed-small loops. In the case of closed-large loops and open field lines, there are very few cases of type down. Hence, the requirement of being up for legs of type II and III is included above to select the vastly dominating population in each case. In Section 3, the results of both the DENT and AWSOM models in the distinct magnetic structures are statistically analysed. As shown in Section 3.1, classification of legs from type 0 through II allows studying the streamer belt in three distinct, progressively outer layers.

2.4. Energy Input Flux

The high temperature of the corona requires heating mechanisms to compensate for the losses. While the vast majority of the existing literature on coronal heating focuses on ARs, some studies have been dedicated to the heating of quiet-Sun regions. In particular, Mac Cormack *et al.* (2017) developed a new application of the DENT technique to estimate the energy input flux required at the base of quiet-Sun coronal loops to maintain them stable. The technique is based on tracing the DENT results along field lines of a global coronal magnetic model, just as described in the previous Section 2.3.

Consider a simple energy balance for each magnetic flux tube, in which the dominating losses of radiative power (E_r) and thermal conduction power (E_c) are compensated by a coronal heating power (E_h) (Aschwanden, 2004):

$$E_h(s) = E_r(s) + E_c(s), \quad (7)$$

where s is the position along the flux tube and the power quantities are in units of $[\text{erg sec}^{-1} \text{ cm}^{-3}]$.

The thermal conduction power E_c equals the divergence of the conductive heat flux F_c , i.e. $E_c(s) = [1/A(s)] d[A(s) F_c(s)]/ds$, where $A(s)$ is the transversal area of the magnetic flux tube at position s . Under a quiescent solar corona plasma regime, the conductive flux is assumed to be dominated by the electron thermal conduction, described by the usual Spitzer model (Spitzer, 1962)

$$F_c(s) = -\kappa_0 T(s)^{5/2} \frac{dT}{ds}(s), \quad (8)$$

where $\kappa_0 = 9.2 \times 10^{-7} \text{ erg sec}^{-1} \text{ K}^{-7/2}$ is the Spitzer thermal conductivity.

Radiative power depends on the amount of plasma in certain temperatures that can radiate. The model estimate it by integrating the squared density multiplied by a radiative loss function $\Lambda(T)$. This function depends on plasma temperature and is calculated by the atomic database and the plasma emission model from CHIANTI (Del Zanna *et al.*, 2015). Then, the expression for radiative power obtained is:

$$E_r = \int dT L_{\text{DEM}}(T) \Lambda(T) \quad (9)$$

The energy balance given by Equation (7) is then integrated in the volume of any given coronal magnetic flux tube. Dividing the result by the flux tube area at the coronal base, and making use of the soleidonal condition of the magnetic field, a field-line integrated version of that energy balance is found,

$$\phi_h = \phi_r + \phi_c. \quad (10)$$

where the line integrated flux quantities $\phi_{r,c}$ [erg sec⁻¹ cm⁻²] are given by (Mac Cormack *et al.*, 2017),

$$\phi_r = \left(\frac{B_0 B_L}{B_0 + B_L} \right) \int_0^L ds \frac{E_r(s)}{B(s)} \quad (11)$$

$$\phi_c = \left(\frac{B_0 F_{c,L} - B_L F_{c,0}}{B_0 + B_L} \right) \quad (12)$$

Note that, for any given field line, all quantities in these two expressions can be computed from the DENT and AWSOM models through Equations (8)-(9). Once computed, the quantity ϕ_h can be calculated, which is the energy input flux required at the coronal base of each coronal field-line to maintain a stable coronal structure.

3. Results

3.1. Tomographic Results

As described in Section 2.1, we carried out DENT reconstructions of the coronal structure for target rotations CR-2082 and CR-2208 using STEREO/EUVI and SDO/AIA data, respectively. Once the LDEM was determined for each rotation, the square root of the mean value of the electron density squared ($\sqrt{N_m^2}$) and the electron mean temperature (T_m) were computed at each voxel of the tomographic computational grid by means of Equations 2 and 3, and the measure R was calculated by means of Equation 4.

As an example, Figures 1 and 2 show latitude-longitude maps of DENT results for both rotations. Three different heights of interest are selected from the tomographic grid, providing also a detailed 3D view of the tomographic results: the lowest height of tomographic **grid** ($1.025 R_\odot$), the lowest height where the AWSOM results are fully consistent with coronal conditions ($1.065 R_\odot$), and a middle height of the tomographic grid ($1.105 R_\odot$). Black voxels correspond to non-reconstructed voxels (see Section 2.1). Thick-black curves indicate the open/closed boundaries of the magnetic field of the AWSOM model.

Both target rotations are highly axisymmetric, i.e. characterized by a high azimuthal symmetry. Rotation CR-2082 showed two small active regions (ARs), both near latitude $+30^\circ$ and around longitudes 50° and 120° , respectively. Rotation CR-2208 showed two ARs, both near latitude $+5^\circ$ and around longitudes 140° and 300° , respectively.

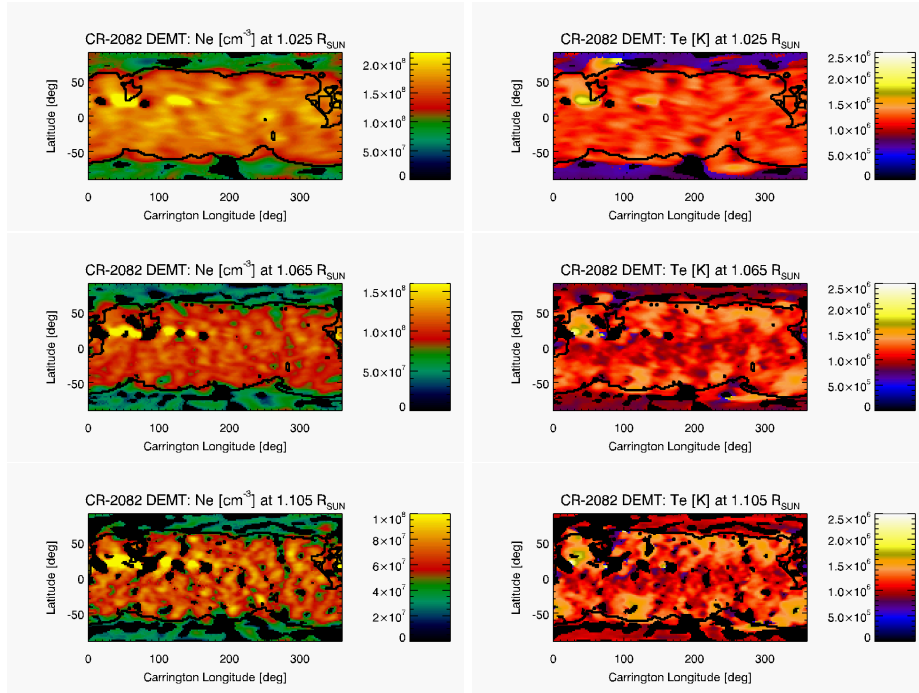


Figure 1. Carrington maps of DMT products $\sqrt{N_m^2}$ (left panels) and T_m (right panels) for CR-2082. Top, middle and bottom panels show the results at three heliocentric heights, 1.025, 1.065 and 1.105 R_{\odot} respectively. Black voxels correspond to non-reconstructed regions (see text in Section 3.1) and thick-black curves indicate the open/closed boundaries.

The magnetically open and closed regions of the AWSoM model are associated to Coronal holes (CHs) and the equatorial streamer belt, respectively. Consistently with that, the location of the open/closed boundaries derived from the respective AWSoM model quite accurately matches the regions of the DMT maps which exhibit the strongest latitudinal gradient of both the electron density and temperature.

Figures 1 and 2 show that the DMT reconstruction of the streamer belt is characterized by relatively larger values of density and temperature in comparison to the CHs. They also show that the streamer belt region of CR-2082 was denser and colder than that of CR-2208. In the case of CR-2082, which belongs to the deep minimum epoch between SCs 24 and 25, the low latitudes of the streamer belt are characterized by lower electron temperature than in its mid-latitudes. A similar behavior is seen in CR-2208, belonging to the declining phase of SC 25, but having a somewhat less axisymmetric structure this characteristic is not so obvious. This thermodynamic structure of the streamer have been reported for other solar minimum rotations in previous DMT works (Lloveras *et al.*, 2017; Nuevo *et al.*, 2013; Vázquez, Frazin, and Manchester, 2010).

For both target rotations, Figure 3 shows latitude-longitude maps of the DMT measure R defined by Equation (4), at the same three heights shown in



Figure 2. Same as Figure 1 but for CR-2208.

Figures 2 and 3. In most of the coronal volume of the DMT grid the agreement between the tomographic and synthetic FBEs is $\lesssim 1\%$. The notable exception is to be found in the CHs of the target rotation analysed based on AIA data. A similar results was found in the two existing DMT works based on data provided by the AIA instrument (Nuevo *et al.*, 2015; Mac Cormack *et al.*, 2017). This point is further discussed below.

To characterize the DMT results in different magnetic structures, we traced $\sqrt{N_m^2}$ and T_m along the magnetic field lines of the AWSoM model. For both rotations, all legss that meet the criteria listed in Section 2.3 were selected. For each leg, the data points of electron density and electron mean temperature as a function of height were fitted to the Equations 5 and 6. As a result, the electron density $N_0(r = 1.0 R_\odot)$ and scale height λ_N were computed for each leg, as well as the temperature gradient $\nabla_r T_m$, and the height-averaged (along the leg) electron temperature $\langle T_m \rangle$.

For both target rotations, the top panels of Figure 4 show the latitude-longitude location (at heliocentric height $r = 1.105 R_\odot$) of all traced field line legs for which criterion (i) of Section 2.3 is met. Open legs are indicated in gray color and closed ones in black color. For each leg, the fits to tomografic temperature and density were applied, as given by Equations (5)-(6). Considering the DMT data points and the resulting fits along each leg, the bottom panels of Figure 4 show the latitude-longitude location of the subset for which also both criteria (ii) and (iii) of Section 2.3 are met. Using a four-color code, type 0, I, II and III

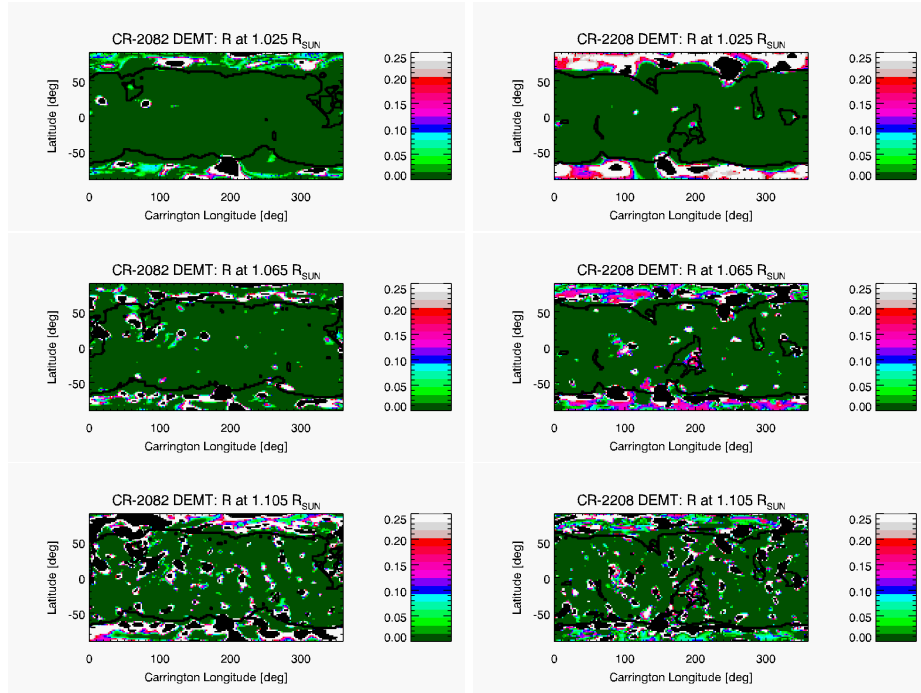


Figure 3. Carrington maps of the measure R defined by Equation (4), for CR-2082 (left panels) and CR-2208 (right panels), at heights 1.025, 1.065 and $1.105 R_{\odot}$, from top to bottom.

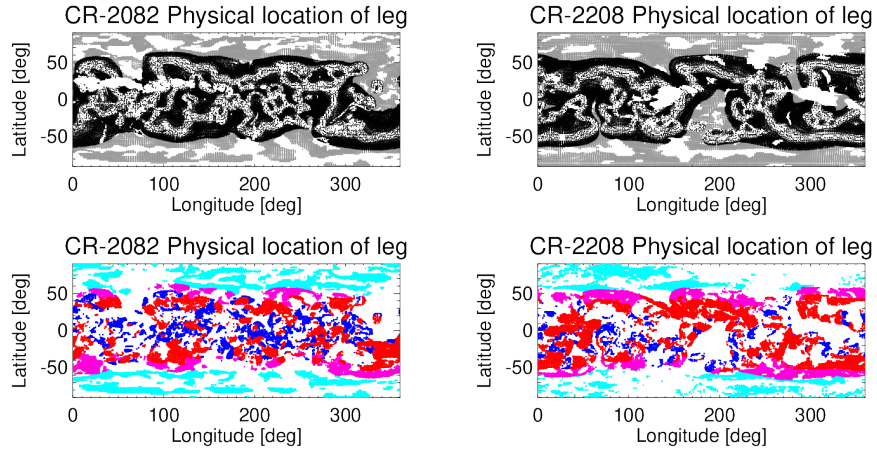


Figure 4. *Top panels:* latitude-longitude location at heliocentric height $r = 1.105 R_{\odot}$ of all open (grey color) and closed (black color) traced field line legs for which criterion (i) of Section 2.3 is met, for both CR2082 (left) and CR2208 (right). *Bottom panels:* latitude-longitude location of the subset for which also both criteria (ii) and (iii) of Section 2.3 are met. The location of type 0, I, II and III legs is shown in blue, red, magenta and cyan color, respectively.

legs are shown in blue, red, magenta and cyan color, respectively. Of the ≈ 44000 legs selected for CR-2082, 20% are type 0, 31% are type I, 23% are type II and 26% type III. On the other hand, of the ≈ 44000 legs selected for CR-2208, 10% are type 0, 43% are type I, 30% are type II and 17% type III.

Type 0 (small down) legs mainly populate the equatorial latitudes. This kind of structure was originally found by Huang *et al.* (2012), and their existence was shown to be anti-correlated with the solar activity level around the solar minimum between SCs 24 and 25 by Nuevo *et al.* (2013). Later on, Lloveras *et al.* (2017) showed that equatorial down loops in streamers were also to be found in the deep minimum between SCs 23 and 24. Here, we verify the existence of this type of structure for the two target rotations. The relatively smaller population of down legs seen in CR-2208, as compared to CR-2082, is consistent with the aforementioned results by Nuevo *et al.* (2013). Type I (small up) mainly populate the mid-latitudes, while type II (large up) legs are mostly very large trans-equatorial field lines forming the envelope of the streamer belt. Finally, type III (open) legs populate the CHs.

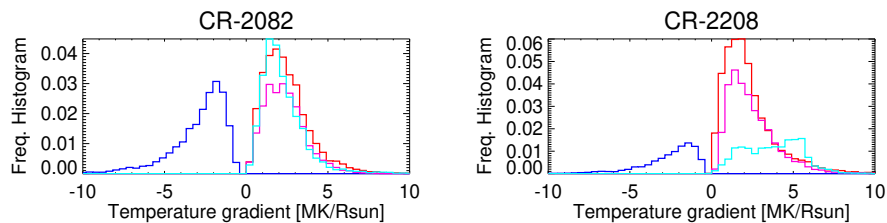


Figure 5. Frequency histograms of the temperature radial gradient for the four types of legs in Figure 4 (using the same color code) for CR-2082 (left panel) and CR-2208 (right panel).

Figure 5 shows frequency histograms $\nabla_r T_m$ for legs of type 0, I, II and III. The lack of population around values close to zero is due to the requirement $|\rho(T, r)| > 0.5$ which discards quasi-isothermal legs. For both rotations, the median value of the temperature radial gradient is $\text{Md}(\nabla_r T_m) \approx -2.5, +2.3$ and $+2.4 \text{ MK/R}_\odot$ for legs of type 0, I and II, respectively.

The notable difference between both rotations is the characteristic value $\text{Md}(\nabla_r T_m) \approx +4.5 \text{ MK/R}_\odot$ for legs of type III for CR-2208. This is related to the much larger R score for the DMT results along CH legs for CR-2208. In this case, DMT performs poorly in modeling a LDEM that predicts the tomographic FBEs with reasonable accuracy. Indeed, visual inspection of the DMT temperature maps for CR-2208 in Figure 3, reveals that in most of the CH region the result for T_m below height 1.105 R_\odot is quite uniform and artificially low. As it turns out, around and above height this height the score R is lower and the temperature results are more reliable. As a result, the temperature gradient along these legs is artificially larger, with the linear fit trying to simultaneously fit the artificially low values of T_m at lower heights. In general, the DMT results in the CH region based on AIA data are thus much less reliable than in the rest of the analysis. We will return to this point in the conclusion section.

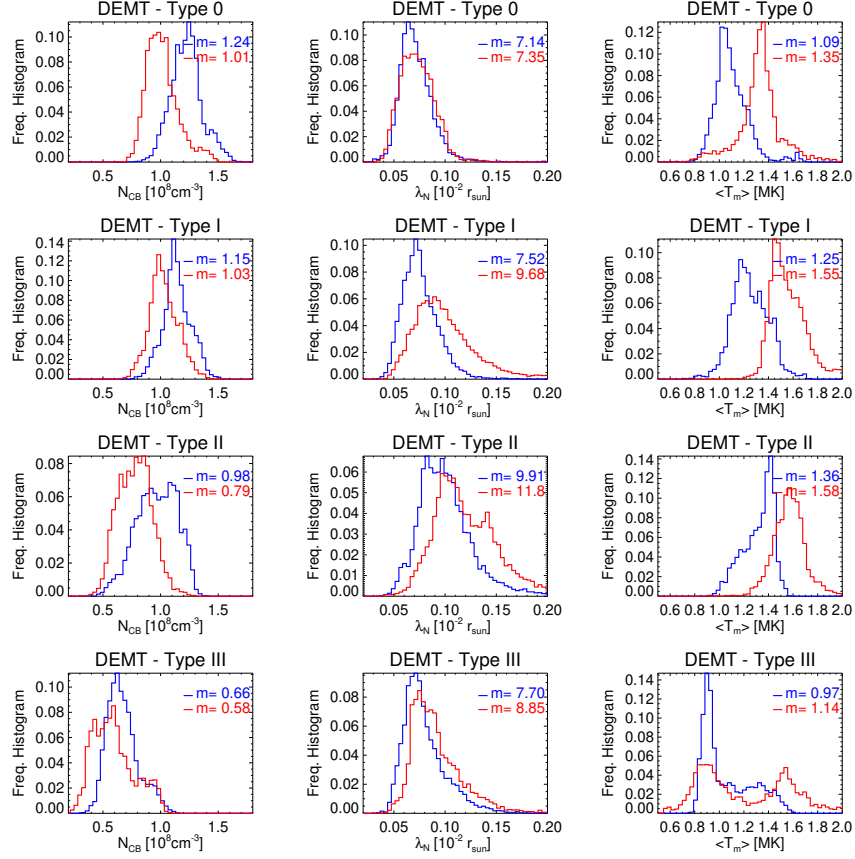


Figure 6. Statistical distribution of DEMENT results for rotations CR-2082 (blue) and CR-2208 (red) traced along legs of type 0, I, II and III (from top to bottom), as defined in Section 2.3. From left to right: electron density $N_{CB} \equiv \sqrt{N_m^2}(r = 1.055 R_\odot)$, electron density scale height λ_N , and loop-averaged temperature $\langle T_m \rangle$. In each panel the median value m is indicated.

For both rotations, Figure 6 shows, in a statistical fashion, the DEMENT results traced along field lines discriminated by leg type. From top to bottom results are shown for type 0 to type III legs, respectively. From left to right the panels show the statistical distribution of $N_{CB} \equiv \sqrt{N_m^2}(r = 1.055)$ (the lowest height where the AWSOM results are consistent with coronal conditions), λ_N and $\langle T_m \rangle$, with the median value m indicated in each plot.

Table 1 summarizes a quantitative comparative analysis between the results of the two target rotations. For CR-2082 quantities are expressed as absolute values, while for CR-2208 they are informed as a percentual variation relative to the corresponding results for CR-2082. The following major results, both concerning the structure of each rotation individually as well as their comparison, can be drawn.

Table 1. Median value (indicated as “Md”) of the statistical distribution of N_{CB} , λ_N , and $\langle T_m \rangle$ for each coronal type of legs defined in Section 2.3. For CR-2082 values are expressed in absolute terms, while for CR-2208 they are informed as a percentual variation relative to the CR-2082 value.

Type	Md(N_{CB}) [10^8 cm^{-3}]	Md(λ_N) [10^{-2} R_\odot]	Md($\langle T_m \rangle$) [MK]
0	1.24 (−19%)	7.1 (+ 3%)	1.09 (+24%)
I	1.15 (−10%)	7.5 (+29%)	1.25 (+24%)
II	0.98 (−20%)	9.9 (+19%)	1.36 (+16%)
III	0.66 (−12%)	7.7 (+15%)	0.97 (+18%)

Throughout the magnetically closed region of both rotations, type 0, I and II legs, associated to increasingly outer regions of the equatorial streamer belt, exhibit progressively decreasing coronal base density, increasing density scale height, and increasing electron temperature. In both rotations also, type III legs in the CHs are characterized by sub-MK temperatures, and electron density values of order $\approx 1/2$ of those observed for the type 0 and type I legs in the core of the equatorial streamer.

A comparison of the results between the two rotations shows that, compared to CR-2082, target rotation CR-2208 was characterized by $\approx 10 - 20\%$ lower values of the electron density at the coronal base, $\approx 5 - 30\%$ larger values of density scale height, and $\approx 5 - 25\%$ larger values of the electron temperature.

To analyze the loop-integrated energy flux quantities introduced in Section 2.3, we selected closed loops for which both legs have the same sign of the radial gradient of the electron temperature $\nabla_r T_m$. In this way, according to the classification of both its legs, each given loop was classified as of type 0 (small down loop), I (small up loop), or II (large up loop). For both target rotations, and for loops of type 0, I and II, Figure 7 shows the frequency histogram of the loop-integrated energy flux quantities ϕ_r , ϕ_c and ϕ_h in blue, green and red color, respectively.

For both rotations, the value of the loop-integrated radiative power E_r , measured by the quantity ϕ_r , is largest for loops of type 0. This is due to $E_r \propto N_e^2 \Lambda(T_e)$, with both factors contributing to maximize E_r for loops of type 0. As shown in Figure 6 and Table 1, loops of type 0 are characterized by the largest values of electron density. Also, in the range of sensitivity of the EUVI and AIA instruments, namely 0.5–3.0 MK (Nuevo *et al.*, 2015), the radiative loss function $\Lambda(T)$ has a local maximum at $T_c \approx 1$ MK. According to Figure 6, loops of type 0, I and II are characterized by values of temperature that are progressively larger and farther from the value T_c , for both rotations.

The sign of the quantity ϕ_c depends on that of the conductive flux F_c . Equations (8) and (12) imply that down loops (type 0) and up loops (type I and II) are characterized by $\phi_c < 0$ and $\phi_c > 0$, respectively, as verified in Figure 7.

Adding the radiative and conductive terms, the characteristic energy input flux at the coronal base is in the range $\phi_h \approx 0.5 - 1.5 \times 10^5 \text{ erg cm}^{-2} \text{ s}^{-1}$,

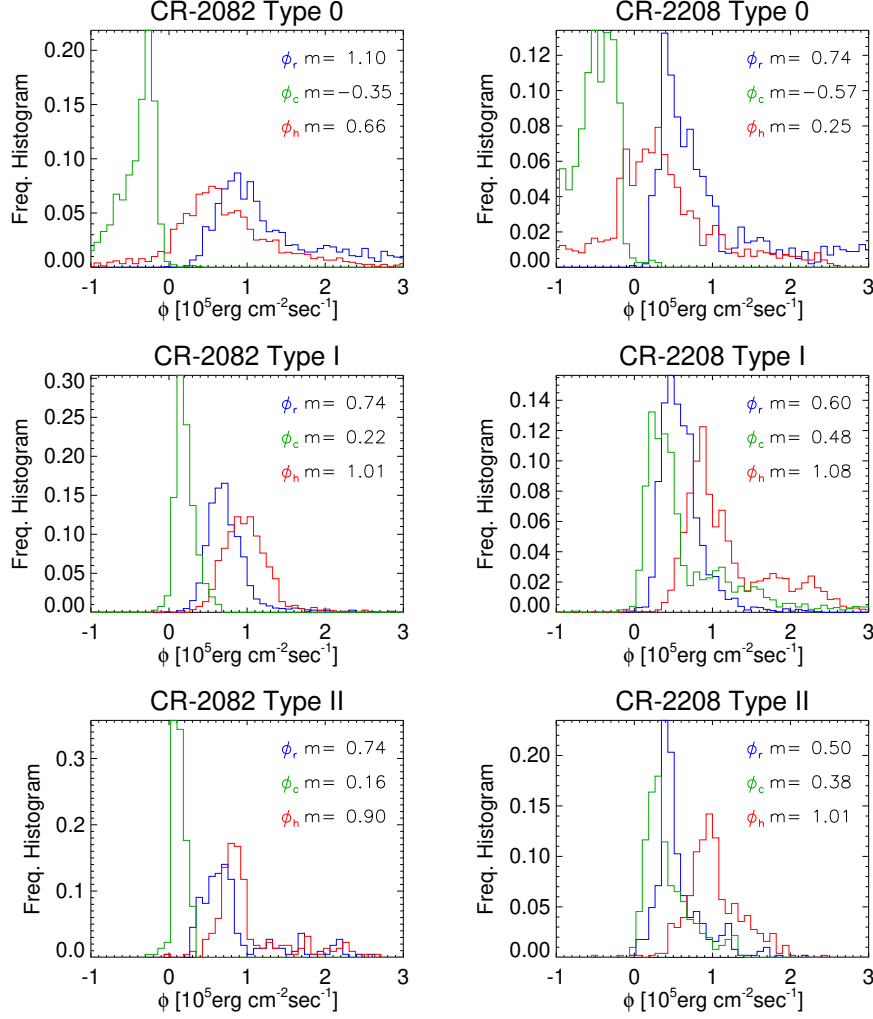


Figure 7. Statistical results of the loop-integrated energy flux quantities ϕ_r , ϕ_c , and ϕ_h in colors blue, red and green, respectively for CR-2082 (left) and CR-2208 (right). From top to bottom, panels show the results for loops of type 0, I and II, which are loops for which both legs meet the criteria from Section 2.3.

depending on the rotation and the type of loop, matching the values reported by Mac Cormack *et al.* (2017). Note that for type 0 loops there is a marginal population characterized by the unphysical result $\phi_h < 0$. As shown by Mac Cormack *et al.* (2017), this affects only the smallest sized loops of the type 0, and it is most probably due to the limited temperature sensitivity of the instrumental passbands. The radiative loss term is here calculated based on plasma emission detected by three coronal bands of EUVI or AIA. Though accounting for most of the coronal plasma, there surely is additional emission out of the instrumental

sensitivity range. As a result, the positive term ϕ_r is most likely underestimated, leading to values $\phi_h < 0$ in loops of type 0, being characterized by $\phi_c < 0$.

3.2. Comparison of the DENT and AWSoM Models

For both target rotations, Figures 8 and 9 show latitude-longitude maps of the AWSoM electron density and temperature. Maps are shown at the same three heights selected for visualization of the DENT results in Figures 1 and 2. Thick-black curves indicate the magnetic open/closed boundaries based on the magnetic field of the AWSoM model. Visual inspection of these maps shows that the AWSoM model for both rotations is highly axisymmetric, as the tomographic model.

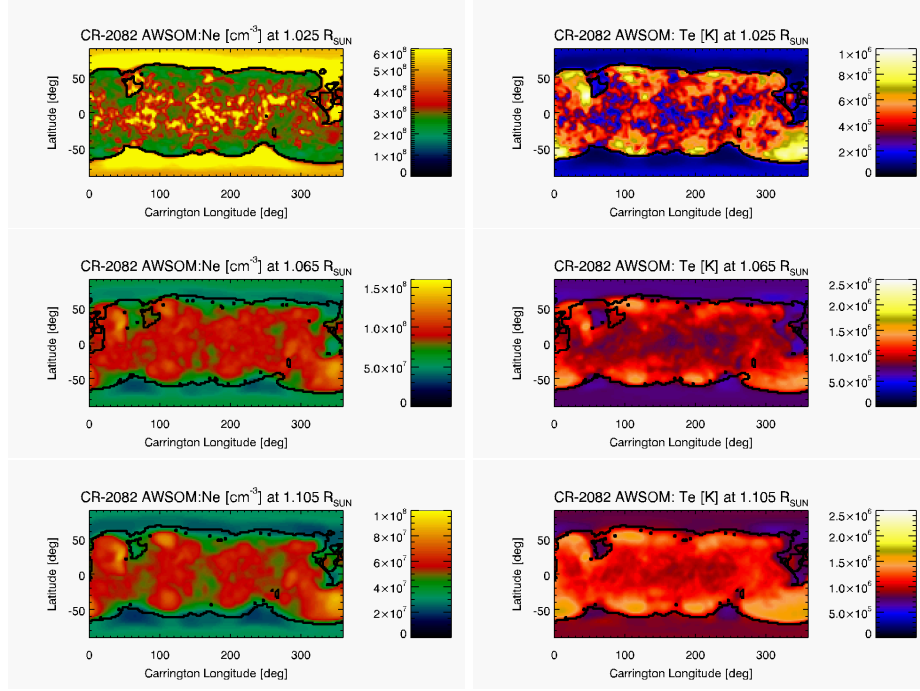


Figure 8. Carrington maps of density (left panels) and temperature (right panels) obtained with AWSoM model for the same three heights shown in Figure 1.

As described in Section 2.2, the AWSoM model includes an artificially thick TR, achieving coronal conditions above height $\approx 1.06 R_{\odot}$. Indeed, the top panels in Figures 8 and 9, at height $1.025 R_{\odot}$, clearly do not represent coronal conditions (although we include them here for completeness). When compared to DENT results (Figures 1 and 2), the latitude-longitude maps of the AWSoM model for heights 1.065 and $1.105 R_{\odot}$ capture well the denser and hotter equatorial streamer belt surrounded by the less dense and colder CHs. Furthermore, for both target rotations, the temperature maps show the low latitudes of the equatorial streamer belt to be characterized by lower temperatures than its mid-latitudes, as also seen in the DENT results. The latitude-longitude maps of the AWSoM and DENT results are shown in the same units and scales, so that a

visual comparison among them already reveals similar values of electron density and temperature in both models.

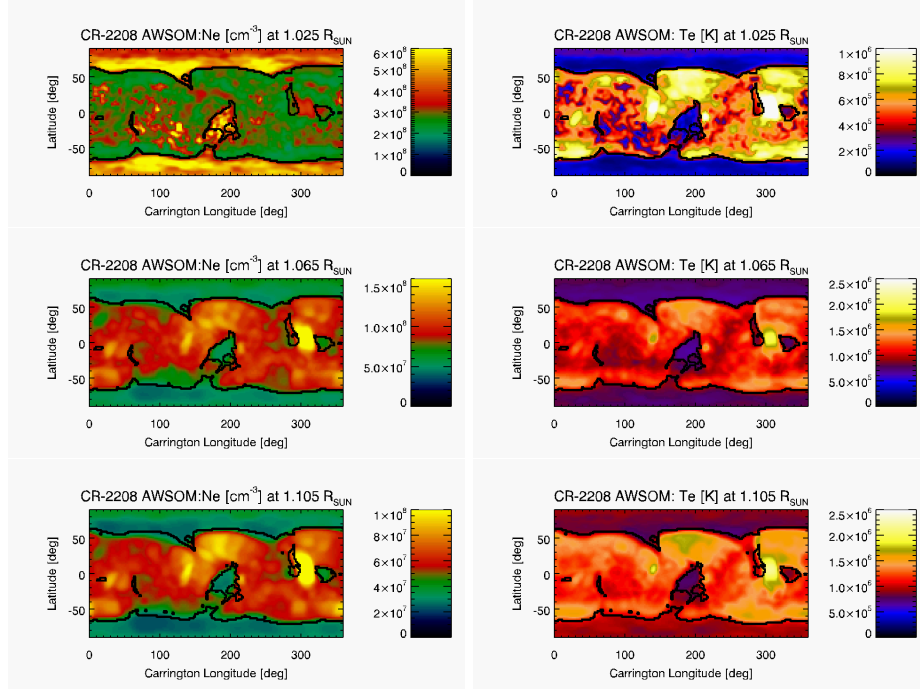


Figure 9. Same as Figure 9 for CR-2208.

Being highly axisymmetric target rotations, the longitude-averaged latitudinal variation of the results of both models is an informative way to compare their large-scale structure. Such comparison is shown in Figure 10 at height $1.105 R_{\odot}$, with top panels comparing electron density and lower panels electron temperature. In these longitude-averaged profiles, longitudes containing ARs or low latitude CHs were excluded. In each panel the averaged latitudinal variation for the DENT model is shown in solid-line style, while the result for the AWSOM model is shown in dashed-linesyle. Left panels show the comparison for CR-2082 (in blue) and right panels for CR-2208 (in red). In each panel the vertical black lines denote the corresponding longitude-averaged latitude of the open-close boundary in both hemispheres.

Several details from Figure 10 are worth being highlighted. Firstly, for CR-2082 the electron density of both models agree within $\approx 20\%$ at all latitudes, and for CR-2208 the agreement is within $\approx 5\%$. In the case of the electron temperature both models agree within $\approx 10-15\%$ at all latitudes for both target rotations. Secondly, for both target rotations, and for both models, these plots clearly show the relatively lower temperatures characterising the low-latitudes of the equatorial streamer belt compared to its mid-latitudes. Thirdly, for both target rotations, the latitude of the open/closed magnetic boundary in both

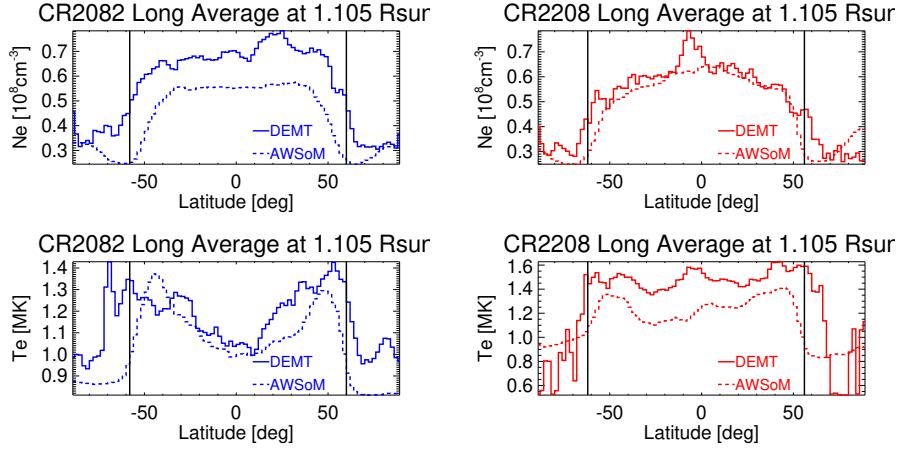


Figure 10. Longitude-averaged latitudinal dependence of the electron density (top) and temperature (bottom) for DMT (blue) and AWSoM (red) results at $1.105 R_{\odot}$. The left (right) panels correspond to CR-2082 (CR2208). The vertical black line indicates the longitude-averaged latitudes of the open/closed magnetic boundary in both hemispheres.

hemispheres matches the location of the strongest latitudinal gradient of the DMT electron density. Note this is not the case for the AWSoM model, that shows a minimum density at the open/closed boundary. Last, note that the DMT electron density decreases from the open/closed boundary towards the poles (in both hemispheres of the two target rotations), while the AWSoM model shows the opposite trend.

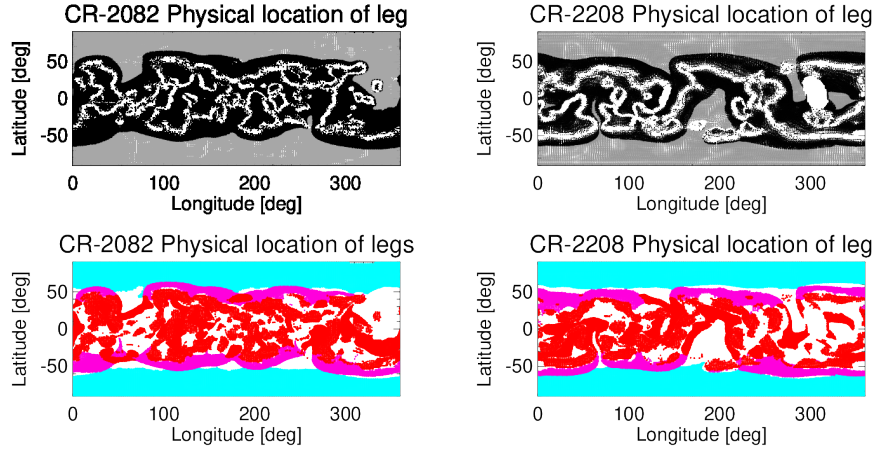


Figure 11. Same as Figure 4, but using the density and temperature of the AWSoM model to classify its legs in types I, II and III. The model does not exhibit legs of type 0.

To characterize the results of the AWSoM model in distinct magnetic structures, its results for electron density and temperature were traced along its magnetic field lines. For each field line leg, the results were then fit to Equations (5) and (6), considering only data points above heliocentric height $1.055 R_{\odot}$. We then classified the traced legs into types I, II and III, according to the criteria described in Section 2.3. Legs of type 0 are not included for AWSoM, as in its current implementation it can not simulate down loops, a point we will discuss in the next section.

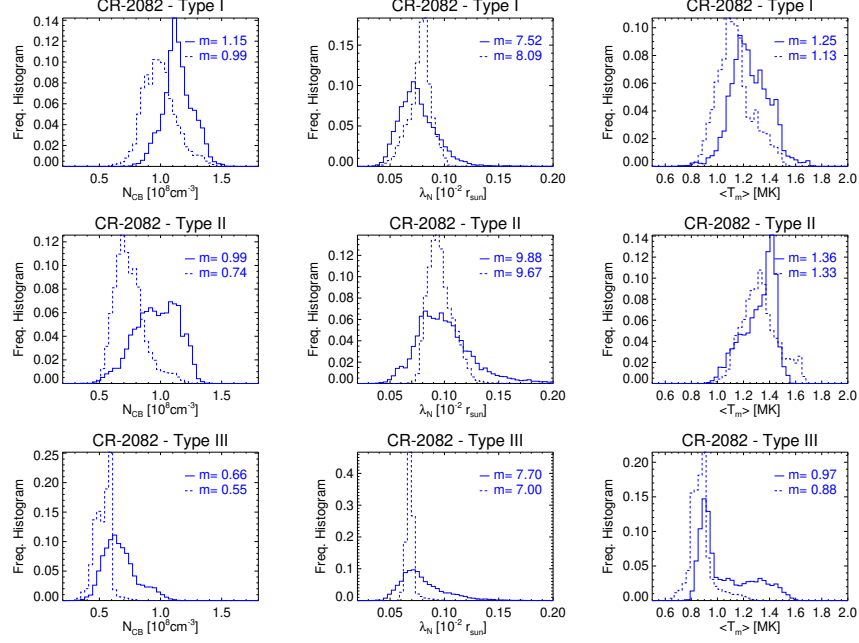


Figure 12. Statistical distribution of the results of the DEMT (solid line-style) and AWSoM (dashed-line style) models traced along legs of type I, II and III (from top to bottom), as defined in Section 2.3. From left to right: electron density at the lowest coronal height of the AWSoM model $N_e(r = 1.055 R_{\odot})$, electron density scale height λ_N , and leg-averaged electron temperature $\langle T_m \rangle$. In each panel the median values m are indicated.

For both target rotations, the top panels of Figure 11 show the latitude-longitude location (at heliocentric height $1.105 R_{\odot}$) of all traced field line legs for which criterion (i) of Section 2.3 is met. That criterion is adapted here, requiring that at least five voxels of the tomographic grid are threaded by the leg. Open legs are indicated in gray color and closed ones in black color. For each leg, the fits to tomographic temperature and density were applied, as given by Equations 5 and 6. Considering the AWSoM data points and the resulting fits along each leg, the bottom panels of Figure 11 show the latitude-longitude location of the subset for which also both criteria (ii) and (iii) of Section 2.3 are met. Using a three-color code, type I, II and III legs are shown in red, magenta and cyan color, respectively. This figure is to be compared with the corresponding Figure

4 for DENT results. It is readily seen that the AWSoM maps are more populated than those of DENT. This is due to the 3D MHD model having electron density and temperature fields spatially smoother than those of DENT.

For target rotation CR-2082, Figure 12 shows the statistical distribution of the results of the DENT (solid line-style) and AWSoM (dashed line-style) models traced along legs of type I, II and III (from top to bottom), as defined in Section 2.3. From left to right: electron density at the lowest coronal height of the AWSoM model $N_{CB} \equiv N_e(r = 1.055 R_\odot)$, electron density scale height λ_N , and leg-averaged electron temperature $\langle T_m \rangle$. In each panel the median values m are indicated. Figure 13 shows the same analysis for target rotation CR-2208.

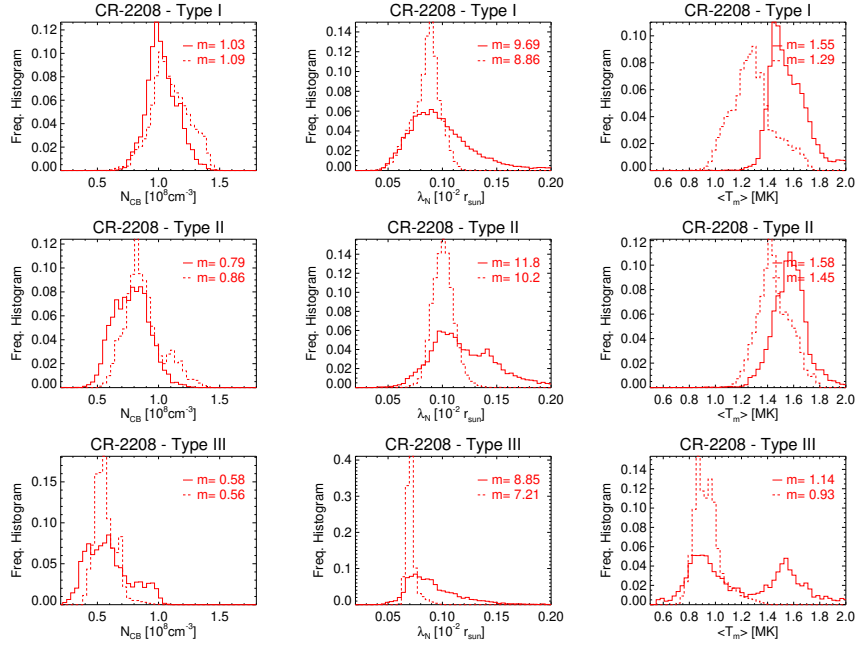


Figure 13. Same as Figure 12 for CR-2208.

For the two target rotations, Table 2 summarizes a quantitative comparative analysis between the results of the DENT and AWSoM models based on the results shown in Figures 12 and 13. The DENT results are expressed as absolute values, while the AWSoM results are informed as a percentual variation relative to the corresponding result for DENT. The following major results can be drawn.

For target rotation CR-2082, the median value of the electron density N_{CB} of both models agree within $\approx 10 - 25\%$, depending of the type of leg, while the median value of the scale height λ_N agree within $\approx 10\%$. The leg-averaged electron temperature $\langle T_m \rangle$ of both models also agree within 10% . For target rotation CR-2208 the agreement of the median value of N_{CB} and λ_N of both models is within 5% , while median values of $\langle T_m \rangle$ agree within 15% . These detailed results informed per magnetic structure are fully consistent with the large-scale comparison provided in Figure 10.

Table 2. Median value (indicated as “Md”) of the statistical distribution of N_{CB} , λ_N , and $\langle T_m \rangle$ for each coronal type of leg defined in Section 2.3. DMT values are expressed in absolute terms, while AWSoM results are informed as a percentual variation relative to the corresponding DMT value.

Type	Md(N_{CB}) [10^8 cm^{-3}]	Md(λ_N) [$10^{-2} R_\odot$]	Md($\langle T_m \rangle$) [MK]
CR-2082			
I	1.15 (-14%)	7.5 (+ 8%)	1.25 (-10%)
II	0.99 (-25%)	9.9 (- 2%)	1.36 (- 2%)
III	0.66 (-17%)	7.0 (- 9%)	0.97 (- 9%)
CR-2208			
I	1.03 (+ 6%)	9.7 (- 8%)	1.55 (-17%)
II	0.79 (+ 9%)	11.8 (-14%)	1.58 (- 8%)
III	0.58 (- 3%)	8.9 (-18%)	1.14 (-18%)

Finally, to provide a graphical comparison of both models across the full range of heliocentric heights covered by the DMT results, Figure 14 shows the average fits of $N_e(r)$ and $T_e(r)$ for legs of type I (red), II (magenta), and III (cyan) for both target rotations. In each panel the DMT and AWSoM results are plotted in solid and dashed line styles, respectively.

As discussed above, Figure 10 shows that the longitude-averaged latitudinal profile of the DMT electron density in the CHs decreases towards the poles. Figure 15 below shows the longitude-averaged AWSoM radial wind speed V_r at $6 R_\odot$, where all field lines are open. The heliocentric current sheet (HCS) location is indicated by the minimum of the speed curve. For each rotation, all velocity data points to the south of the HCS position map down to the southern CH in Figures 10. Similarly, all velocity data points to the north of the HCS position map down to the northern CH in Figures 10. This clearly shows an anti-correlation between the DMT electron density at low heights and the AWSoM wind speed at larger heights.

NOTE: We could quantify the anti-correlation between the AWSoM terminal speed and the DMT electron density at the coronal base in the following fashion. We can set up starting points at, say, $20 R_\odot$, every one degree, both in latitude and longitude. This would mean setting up 180×360 starting points. We trace then the (open) field lines from each of those starting points down to $1.0 R_\odot$ to find out the DMT results at those lower heights for each field line. Now, to do this we need to develop some codes and have no time for this paper. We can postpone it for a next effort, or... Chip: do you think you could do this with your present tools? Do you think it is interesting? I think so. Our submission deadline is 24 January.

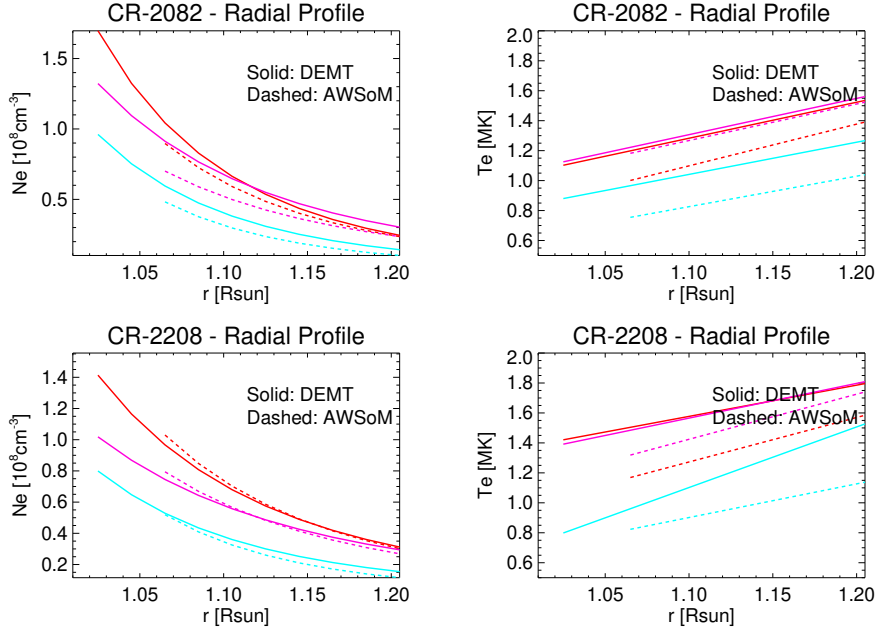


Figure 14. Average fits to $N_e(r)$ (left panels) and $T_e(r)$ (right panels) for legs of type I (red), II (magenta), and III (cyan), for CR-2082 (top panels) and CR-2208 (bottom panels). Solid lines correspond to DGMT results while dashed lines correspond to AWSOM results.

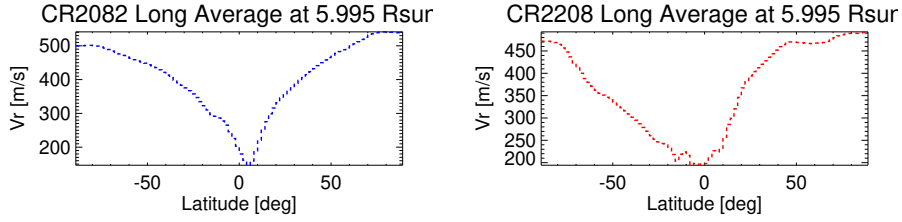


Figure 15. Longitude-averaged latitudinal dependence of the AWSOM model wind speed at $6.0 R_\odot$ for CR2082 (left panel) and CR2208 (right panel). **NOTE:** (by Albert): Even if this is not yet the terminal speed, it is a pretty high height, and one can already see the transition from FAST to SLOW speed in the model, where the absolute minimum indicates the location of the HCS at this height. I believe it is interesting to compare these two curves with Figure 10. Note that while in this Figure all latitudes are magnetically open, in Figure 10 only the part at latitudes larger than the vertical black lines are open. Note that DGMT shows that in the open low corona N_e decreases from the O/C boundary towards the poles, anti-correlating with the AWSOM terminal speed, which is nice. In order to quantify this anti-correlation we need to trace the terminal speed and the DGMT N_e , which we may need to do with the help of Chip and Nishtha. Chip, we can discuss this idea over Skype after Xmas if you are around.

4. Discussion and Conclusions

We carried out the 3D DENT reconstruction and MHD modeling of the inner solar corona for two target rotations, CR-2082 and CR-2208. The first target belongs to the deep minimum epoch between SCs 23 and 24, while the latter belongs to the end of the declining phase of SC 24. The present work introduces two improvements in the implementation of DENT, namely the use of only off-limb data in the EUV images, and the inclusion of a 3D regularization scheme. As a result of the former, artifacts introduced by coronal dynamics are mitigated, and as a result of the latter, tomographic reconstructions behave more smoothly close to the radial boundaries of the computational grid when compared to previous reconstructions. The MHD model used is here the latest version of the AWSoM component of the SWMF suite.

Based on the magnetic field model of AWSoM model and the results of the DENT model for electron density and temperature, we classified coronal structures in four different types. Smaller legs in the core of the streamer belt are classified in down/up types according to their temperature decreasing/increasing with height (dubbed type 0/I). Larger closed legs of type up that form the envelope of the streamer belt (dubbed type II), and open field lines of type up populating the CHs (dubbed type III).

Concerning the DENT reconstructions, throughout the magnetically closed region of both rotations, we find that type 0, I and II legs are associated to increasingly outer regions of the equatorial streamer belt, and exhibit progressively decreasing coronal base density, increasing density scale height, and increasing electron temperature. For both target rotations we find that down legs populate the low latitudes of the streamer belt, while up legs dominate its mid-latitudes. Also, in the case of CR-2082 the fraction of down legs is significantly larger than for CR-2208. These findings are consistent with previous studies by Huang *et al.* (2012) and Nuevo *et al.* (2013). In the case of the latter, they include in their analysis target CR-2081, which is a rotation almost identical to our target CR-2082. Our results for target CR-2082 compare very well with those of Nuevo *et al.* (2015) and Lloerveras *et al.* (2017) for target CR-2081. As our study uses the improved version of the DENT technique, such comparison provided a consistency check for the changes implemented in the DENT technique.

In both rotations also, type III field lines in the CHs are characterized by sub-MK temperatures, and electron density values of order $\approx 1/2$ of those observed for the type 0 and type I lines in the core of the equatorial streamer. In the case of the AIA based DENT reconstruction, we show that in a substantial fraction of the CHs region the technique performs poorly in modeling LDEMs that predict the tomographic emissivity in each EUV band with reasonable accuracy. As a result, DENT results based on AIA data are currently less reliable in the CH region. This was already found by the existing two previous DENT works based on AIA data (Nuevo *et al.*, 2015; Mac Cormack *et al.*, 2017). The source of this distinct performance of DENT when applied to EUVI or AIA data is related to the TRFs of the respective filter sets. We are currently implementing an improved LDEM determination algorithm to deal with this issue that will be used in a follow up article.

In comparing the DENT results obtained for the two selected targets, we highlight here that they rely on data provided by two different instruments, namely EUVI and AIA for CR-2082 and CR-2208, respectively. In order to quantify the systematic difference of the DENT products based on both instruments, Nuevo *et al.* (2015), who were the first to apply DENT to AIA data, analysed a single target using both instruments independently. They found that while the density products are essentially equal, the temperature product of DENT based on AIA data is systematically 8% larger than the one based on EUVI data, i.e. $T_m^{(\text{AIA})}/T_m^{(\text{EUVI})} \approx 1.08$. Considering such correction, Figure 6 and Table 1 indicate that CR-2208 was characterized by temperatures $\approx 10 - 15\%$ larger relative to CR-2082 throughout the streamer belt region. As for the electron density products, CR-2208 was found to be $\approx 15 - 20\%$ less dense than CR-2082 throughout the streamer belt region. These systematic differences are around or beyond the uncertainty level in the DENT products due to systematic sources (radiometric calibration and tomographic regularization), that Lloveras *et al.* (2017) estimated to be $\Delta T_m \approx 10\%$ and $\Delta \sqrt{N_m^2} \approx 5\%$.

In the streamer belt region we combined the DENT results and the AWSoM magnetic model to infer the energy input flux ϕ_h at the coronal base required to maintain stable coronal loops. To this end, we applied the technique developed by Mac Cormack *et al.* (2017). We found characteristic values in the range $\phi_h \approx 0.5 - 1.5 \times 10^5 \text{ erg cm}^{-2} \text{ s}^{-1}$, depending on the rotation and the type of loop, matching the values reported by Mac Cormack *et al.* (2017). Based on spectroscopic data of the EIS instrument in quiet-Sun regions Hahn and Savin (2014) showed that, if the observed non-thermal broadening are assigned to Alfvén waves, their energy flux at the coronal base is estimated to be in the range $\approx 1.5 - 2.5 \times 10^5 \text{ erg cm}^{-2} \text{ s}^{-1}$. A large fraction of the coronal base energy input flux ϕ_h estimated in this work, or even its totality, could then be accounted for by Alfvén waves.

Results of the AWSoM model are compared to those of the DENT reconstructions in the range of coronal heights $\approx 1.05 - 1.20 R_\odot$ simultaneously covered by both models. In its current implementation, the AWSoM model can not reproduce down loops (type 0), so the comparison is restricted to type I, II and III field lines. The detailed comparison shown in this work can be summarized as follows. For CR-2082, the electron density of both models agree within $\approx 20\%$ in all regions, while for CR-2208 the agreement is within $\approx 5\%$. In the case of the electron temperature, both models agree within $\approx 10 - 15\%$ in all regions, for both target rotations. This level of agreement between both models is considerably better than that reported in previous works. Oran *et al.* (2015) and Jin *et al.* (2012) reported electron density values of the AWSoM model typically 50% larger than those of the DENT reconstructions. [NOTE: Chip, if Section 2.2 explains the most significant improvements of AWSoM since the version used in those references, we can comment on the reason for the improvement here.](#)

Within the quantitative match summarized in the previous paragraph, there are some qualitative agreements and disagreements between both models worth noticing. For both target rotations, the AWSoM model reproduces the relatively lower temperatures found by DENT to characterize the low-latitudes of the equatorial streamer belt compared to its mid-latitudes. On the other hand, while

the latitude of the open/close magnetic boundary in both hemispheres matches the location of the strongest latitudinal gradient of the DENT electron density, this is not the case for the AWSOM model, that shows a minimum density at the open/closed boundary. Also, while the DENT electron density decreases from the open/closed boundary towards the poles (in both hemispheres of the two target rotations), the AWSOM model shows the opposite trend. This behavior is notoriously opposite to that reported in the AWSOM model version used by Oran *et al.* (2015), in which the electron density decreases from the open/closed boundary towards the poles. **NOTE: Chip: Even if the match AWSOM/DENT is quantitatively pretty good, this qualitative opposite behavior is off putting. Do you think there is room for improvement in the AWSOM model here? Maybe worth mentioning?**

NOTE: Chip: In relation to the previous comment, if the analysis proposed in Figure 15 is carried out we should say something about that here.

A detailed empirical description of the 3D thermodynamic structure of the inner corona at a global scale is currently only possible with tomographic techniques, such as DENT. Using tomographic results for continuous validation of 3D MHD models is of high relevance for the continued improvement of models. In a follow up article we will analyse with DENT and 3D MHD modeling new target rotations of the current solar minimum between SCs 24 and 25, in particular the rotations corresponding to the 2019 and 2020 total solar eclipses.

NOTE: Diego, agregá las sección de agradecimientos, fijándote como lo hicimos para tu paper anterior. Vos seguro debes agradecer a la beca, Ceci tambien (fijate en su paper), y todos los de aquí deberemos agradecer grants. Armalo como puedas y luego lo revisamos.

Acknowledgments D.G.LL. and C.M.C. acknowledges CONICET doctoral fellowship (Res. Nr. 4870) to IAFE that supported his participation in this research. The authors acknowledge ANPCyT grant 2012/0973 and CONICET grant PIP # 11220120100403 *estos son viejos?* to IAFE that partially supported their participation in this research

References

- Aschwanden, M.J.: 2004, *Physics of the Solar Corona. An Introduction*. ADS.
- Aschwanden, M.J., Schrijver, C.J.: 2002, Analytical Approximations to Hydrostatic Solutions and Scaling Laws of Coronal Loops. *Astrophys. J. Suppl.* **142**(2), 269. DOI. ADS.
- Del Zanna, G., Dere, K.P., Young, P.R., Landi, E., Mason, H.E.: 2015, CHIANTI - An atomic database for emission lines. Version 8. *Astron. Astrophys.* **582**, A56. DOI. ADS.
- Frazin, R.A.: 2000, Tomography of the Solar Corona. I. A Robust, Regularized, Positive Estimation Method. *Astrophys. J.* **530**, 1026. DOI. ADS.
- Frazin, R.A., Vázquez, A.M., Kamalabadi, F.: 2009, Quantitative, Three-dimensional Analysis of the Global Corona with Multi-spacecraft Differential Emission Measure Tomography. *Astrophys. J.* **701**, 547. DOI. ADS.
- Hahn, M., Savin, D.W.: 2014, Evidence for Wave Heating of the Quiet-Sun Corona. *Astrophys. J.* **795**(2), 111. DOI. ADS.
- Huang, Z., Frazin, R.A., Landi, E., Manchester, W.B., Vázquez, A.M., Gombosi, T.I.: 2012, Newly Discovered Global Temperature Structures in the Quiet Sun at Solar Minimum. *Astrophys. J.* **755**, 86. DOI. ADS.
- Jin, M., Manchester, W.B., van der Holst, B., Oran, R., Sokolov, I., Toth, G., Gombosi, T.I., Vourlidas, A., Liu, Y., Sun, X.: 2012, Simulate the Coronal Mass Ejection on 2011 March 7 from Chromosphere to 1 AU. In: *AGU Fall Meeting Abstracts* **2012**, SH33E. ADS.

- Landi, E., Young, P.R., Dere, K.P., Del Zanna, G., Mason, H.E.: 2013, CHIANTI - An Atomic Database for Emission Lines. XIII. Soft X-Ray Improvements and Other Changes. *Astrophys. J.* **763**, 86. DOI. ADS.
- Lloveras, D.G., Vázquez, A.M., Nuevo, F.A., Frazin, R.A.: 2017, Comparative Study of the Three-Dimensional Thermodynamical Structure of the Inner Corona of Solar Minimum Carrington Rotations 1915 and 2081. *Solar Phys.* **292**(10), 153. DOI. <https://doi.org/10.1007/s11207-017-1179-z>.
- Mac Cormack, C., Vázquez, A.M., López Fuentes, M., Nuevo, F.A., Landi, E., Frazin, R.A.: 2017, Energy Input Flux in the Global Quiet-Sun Corona. *Astrophys. J.* **843**, 70. DOI. ADS.
- Nuevo, F.A., Huang, Z., Frazin, R., Manchester, i. Ward B., Jin, M., Vázquez, A.M.: 2013, Evolution of the Global Temperature Structure of the Solar Corona during the Minimum between Solar Cycles 23 and 24. *Astrophys. J.* **773**(1), 9. DOI. ADS.
- Nuevo, F.A., Vázquez, A.M., Landi, E., Frazin, R.: 2015, Multimodal Differential Emission Measure in the Solar Corona. *Astrophys. J.* **811**(2), 128. DOI. ADS.
- Oran, R., Landi, E., van der Holst, B., Lepri, S.T., Vázquez, A.M., Nuevo, F.A., Frazin, R., Manchester, W., Sokolov, I., Gombosi, T.I.: 2015, A Steady-state Picture of Solar Wind Acceleration and Charge State Composition Derived from a Global Wave-driven MHD Model. *Astrophys. J.* **806**(1), 55. DOI. ADS.
- Press, W.H., Teukolsky, S.A., Vetterling, W.T., Flannery, B.P.: 2002, *Numerical recipes in C++ : the art of scientific computing*. ADS.
- Schiff, A.J., Cranmer, S.R.: 2016, Explaining Inverted-temperature Loops in the Quiet Solar Corona with Magnetohydrodynamic Wave-mode Conversion. *Astrophys. J.* **831**(1), 10. DOI. ADS.
- Serio, S., Peres, G., Vaiana, G.S., Golub, L., Rosner, R.: 1981, Closed coronal structures. II - Generalized hydrostatic model. *Astrophys. J.* **243**, 288. DOI. ADS.
- Spitzer, L.: 1962, *Physics of Fully Ionized Gases*. ADS.
- Vázquez, A.M.: 2016, Seeing the solar corona in three dimensions. *Advances in Space Research* **57**, 1286. DOI.
- Vázquez, A.M., Frazin, R.A., Kamalabadi, F.: 2009, 3D Temperatures and Densities of the Solar Corona via Multi-Spacecraft EUV Tomography: Analysis of Prominence Cavities. *Solar Phys.* **256**(1-2), 73. DOI. ADS.
- Vázquez, A.M., Frazin, R.A., Manchester, I. Ward B.: 2010, The Solar Minimum Corona from Differential Emission Measure Tomography. *Astrophys. J.* **715**(2), 1352. DOI. ADS.